Perfect splitting in rectangular-waveguide junctions for analog computing

William Rogers[1,†] Christian Johnson-Richards[1,†] Alex Yakovlev[2] and Victor Pacheco-Peña[1,*]

[1]*School of Mathematics, Statistics and Physics, Newcastle University, Newcastle upon Tyne, NE1 7RU, United Kingdom*

[2]*School of Engineering, Newcastle University, Newcastle upon Tyne, NE1 7RU, United Kingdom*

It has recently been shown how computing operations such as high-speed switching, routing, and solving partial differential equations can be performed by exploiting perfect splitting of electromagnetic waves in networks of waveguides from microwaves to the optical regime. Here we propose a technique to achieve perfect splitting of electromagnetic waves using junctions of rectangular waveguides. The structure consists of N air-filled rectangular waveguides interconnected at a junction. They are designed to have their cutoff frequency above the cutoff frequency of a further N waveguides used as inputs. The proposed structure is studied theoretically with use of transmission-line models, and it is demonstrated that perfect splitting can occur at frequencies below the cutoff frequency of the interconnected waveguides (evanescent coupling). Numerical results are used to validate the designs, and it is demonstrated that the theoretical model fits the numerical data well. As examples of computing operations, it is shown how the proposed structure can be used to compare the amplitude of two incident signals (comparison operation) and also for routing of information to different output ports by exploiting the linear superposition of scattered waves excited at the junction of rectangular waveguides, opening new opportunities and possibilities for future exploration and exploitation of electromagnetic waves for high-speed computing.

I. INTRODUCTION

The increasing need for powerful and faster computing systems has pushed the field of computing to evolve at an unprecedented speed. However, challenges in the performance and manufacturing of integrated-circuit chips (e.g., chips are approaching physical size limits [1,2]) need to be tackled to fulfill demands [3]. Classical computing systems, such as digital electronics, rely on a large number of transistors as switching devices. However, inherent to such devices are unavoidable parasitic capacitances that appear at their gate. The charging and discharging of these capacitances during switching introduce delays and can cause energy dissipation, reducing the overall performance of the computing system [4]. While there is ongoing research to address these challenges, there is growing interest in the development of alternative computing paradigms, giving

rise to interesting examples such as quantum [5], biological [6] and photonic [7–15] computing approaches.

Within the realm of photonic computing, recent examples in this field include methods for solving quadratic optimization problems and multivariate equations [7,16], differentiation and integration [8–12], optical neural networks [13,17–19], and the solving of partial differential equations with interconnected-waveguide junctions [20,21]. Moreover, optical logic gates and circuits have been demonstrated using inverse design [22] and plasmonic structures [23]. We have also seen work demonstrating how this paradigm may offer opportunities for low-power, high-speed digital and analog computations [24–33]. Recently, a technique that has been used for computational purposes is perfect splitting of electromagnetic (EM) waves within junctions of waveguides. In this technique, EM waves split following the scattering matrix represented by interconnected ideal transmission lines (TLs) for an N-port junction considering waveguides of equal impedance [34,35]. Perfect splitting differs from typical power splitting because reflections are present at the incident port, which is a result of the structures emulating ideal interconnected TLs. Interestingly, these reflections are needed for computing within larger network of waveguides. In this context, we have recently shown how ideal splitting of EM signals between a

---

junction of four-port parallel-plate waveguides can be used for elementary computing operations such as information routing and comparison operations [34,36], which provides a fundamental pathway for elementary decision-making computations. A similar approach using plasmonic junctions at optical frequencies has also been demonstrated [37]. Further examples include the calculation of temporal derivatives and solutions for partial differential equations using interconnected-waveguide junctions [18,19] as well as emulation of Kirchhoff's law in photonics [38]. Perfect splitting in a four-port waveguide junction, as an example, requires an incoming signal applied from one of the waveguides to be split into four signals after passing the junction. Each signal (traveling within each of the waveguides) will have the same magnitude with phase difference π between the reflected signal (traveling towards the incident port) and the transmitted signals (traveling towards the other three ports) [35] (full details about such perfect splitting in N-port-waveguide networks are given in the following sections). Such waveguide junctions require a large incident-wavelength-to-waveguide-width ratio for them to be considered as perfect (ideal) TLs, and this is the reason why they have been implemented mainly via parallel-plate waveguides [34,36,39,40]. Parallel-plate waveguides allow operation at incident wavelengths much longer than the width of the waveguide. However, a main drawback of parallel-plate waveguides is that, when one is considering realistic waveguides with finite dimensions along the transverse axis, fringing fields at the edge of the parallel plates can appear, affecting their performance as ideal TLs, as shown in Ref. [41]. Alternative efforts to achieve perfect splitting of EM waves include the use of scattering particles at the center of a junction or the use of plasmonic waveguides and dielectric structures [37,40]. Here we build upon these studies to enable elementary computing operations by implementing arrays of rectangular waveguides as realistic and technologically relevant structures. As in the ideal configurations, our work also relies on perfect splitting of EM waves at a waveguide junction. The challenge, however, is that the large wavelength-to-waveguide-width ratio, required to mimic ideal TLs for perfect splitting [26], is limited when one is working with rectangular waveguides. This is due to their width (along the direction perpendicular to the electric field) being linked to the cutoff wavelength of the fundamental TE$_{10}$ mode, meaning that small cross sections cannot be achieved [35]. Hence, when one is simply interconnecting rectangular waveguides to create a junction, perfect splitting cannot occur (as discussed below). However, this could be addressed using alternative waveguide junctions with rectangular waveguides of carefully designed cross sections.

Inspired by the importance of photonic computing and the need for perfect splitting in arrays of interconnected waveguides, here we present our efforts to achieve perfect splitting of incident EM signals within a four-port network of rectangular waveguides operating below their fundamental TE$_{10}$ mode. The structure consists of four vacuum-filled rectangular waveguides designed to have their cutoff frequency at f_{c_w} (called "outer waveguides"). These waveguides are interconnected via a cross-junction comprising four vacuum-filled rectangular waveguides having a higher cutoff frequency, $f_{c_x} > f_{c_w}$ (called "junction waveguides"). In so doing, we show how perfect splitting of EM waves can be achieved at frequencies that fall above the cutoff frequency of the outer waveguides but below the cutoff frequency of the junction waveguides (i.e., evanescent coupling). The mechanisms enabling such perfect splitting are presented and studied via numerical simulations with CST Studio Suite®. To understand this performance, in-depth analytical studies using TL theory are presented. It is shown how the reactive field at the junction can be modeled via a reactive element, demonstrating how there are frequencies where perfect splitting is achieved even below the cutoff frequency of the junction waveguides, leading to a model that closely fits the numerical simulations. For completeness, we show how the proposed configuration using rectangular waveguides can be exploited for N-port perfect splitting. Finally, we implement the proposed structure to perform some computing operations, including elementary signal routing and amplitude-comparison operations.

II. PRINCIPLES OF PERFECT SPLITTING AND PROPOSED STRUCTURE

A. Definition of perfect splitting

As mentioned in Sec. I, perfect splitting of EM signals has recently been used for fundamental computing operations such as routing of information [34,36,42]. A detailed explanation of the implications of perfect splitting using interconnected TLs can be found in Ref. [34], but a summary is provided here for completeness. A schematic representation of the concept of perfect splitting of EM signals considered in this work is presented in Fig. 1, where it is shown how an incident signal applied from port 1 is split into N signals, each of them traveling towards each of the ports connected to the ideal splitter. Note that the concept of perfect splitting considered here is different from that of multiport power dividers, where the incident signal is equally divided and delivered to the $N - 1$ output ports of a network without reflection [43]. Here, however, a reflected signal travelling towards port 1 will also be necessary for consideration as perfect splitting. Interestingly, while reflections are usually unwanted in devices from microwave to photonic applications, it has been shown that perfect splitters that use both transmitted and reflected signals can be applied to computing processes such as routing of information, calculation of derivatives in the time domain, emulation of Kirchhoff's law in photonics,
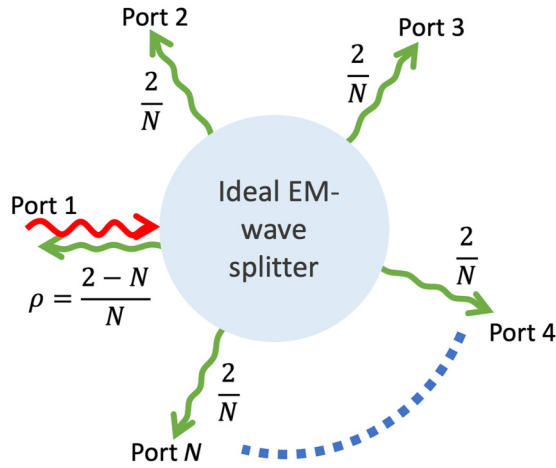
FIG. 1.   An ideal splitter in a N-port device.

and the calculation of the solution of partial differential equations [20,34,36,38], to name a few. A perfect splitter can be designed by use of ideal TLs interconnected at a junction either in series or in parallel [36,42]. From TL theory [35], if all the interconnected TLs have the same impedance, $Z_1 = Z_2 = Z_3, \ldots, Z_N = Z$, the incident signal applied from port 1 (TL with impedance Z_1) will see a change of impedance from $Z_1 = Z$ to $Z_{\mathrm{out}} = (N-1)Z$ or $Z_{\mathrm{out}} = [(N-1)/Z]^{-1}$ if the TLs are interconnected in series or in parallel, respectively. In this way, transmitted and reflected signals will be travelling towards the output and input ports, respectively, with a transmission coefficient and a reflection coefficient (for each port) defined as $\gamma = -2N^{-1}$ and $\rho = (N-2)N^{-1}$, respectively, if the TLs are interconnected in series, or $\gamma = 2N^{-1}$ and $\rho = (2-N)N^{-1}$, respectively, if they are connected in parallel (the latter case is depicted in Fig. 1).

Note that the signs of γ and ρ have been written to directly account for the change of phase of the transmitted and reflected signals [34]. Importantly, for the case when four TLs are interconnected in a parallel configuration (as it is the case in the next section), the reflected signal has the same amplitude, but it is 180° (π) out of phase with the transmitted signals.

If multiple signals are applied from different ports, one can simply exploit the linearity of the system and consider that the output signals transmitted towards each port will be the superposition of the scattered signals excited after each of the input EM signals has passed the junction, i.e., for an input vector of EM signals $\mathbf{x} = [x_1, x_2, \ldots, x_N]$, with the subscript indicating the port number, an output vector of EM signals $\mathbf{y} = [y_1, y_2, \ldots, y_N]^T$ can be defined. This means that for the case of N TLs interconnected in series or in parallel, $\mathbf{y}$ can be simply calculated by one multiplying an $N \times N$ scattering matrix with diagonal and off-diagonal terms representing the reflection coefficient and the transmission coefficient of the junction, respectively, and the

input vector of signals as

$$
\mathbf{y} = \begin{pmatrix} \rho & \gamma & \gamma & \cdots \\ \gamma & \rho & \gamma & \cdots \\ \gamma & \gamma & \rho & \gamma \\ \vdots & \vdots & \gamma & \ddots \end{pmatrix} \mathbf{x}^T , \qquad (1)
$$

with T as the transpose operator. To implement the perfect-splitting theory described above and to use it for computing operations, one can use waveguides as TLs [35]. However, for them to behave as ideal TLs (without exciting fringing fields at the junction), it is required to have a much greater incident wavelength of the EM signal compared with the cross section of the waveguide. It has been shown that when this ratio exceeds approximately 8:1, interconnected waveguides can mimic ideal interconnected TLs [39]. This is possible with, for instance, parallel-plate waveguides, where the distance between the metallic plates can be reduced to fulfill this condition. However, parallel-plate waveguides interconnected at a junction are ideal structures that require—for instance, when connected in series—infinitely long plates along the direction orthogonal to the propagation of the EM signals. This is to avoid fringing fields at the edges of the waveguides and at the junction (i.e., ideal two-dimensional structures). One may ask whether there is a way to emulate perfect splitting using rectangular waveguides instead, as examples of technologically relevant structures. At first glance, one can envision that this can become a challenge provided that the dimensions of the rectangular waveguides are on the order of the cutoff wavelength λ_c of the fundamental TE_{10} mode. TE modes exist only when the incident signal wavelength, λ, is less than λ_c. The cutoff wavelength (and hence frequency) of the first TE_{10} mode, λ_c, is defined by the width a of the waveguide (dimension transverse to the direction of the electric field) as $\lambda_c = 2a$ [35]. Subsequently, the cutoff wavelength limits the maximum wavelength-to-waveguide-width ratio to 2:1 when one is working near the cutoff. To demonstrate this, an example showing four interconnected waveguides at a junction is shown as Supplemental Material [44], demonstrating how there are no frequencies above the cutoff frequency of the fundamental mode where perfect splitting can be achieved, as expected. On this basis, is there a possibility to overcome this using rectangular waveguides? In the following section, we address this question by proposing an alternative configuration for interconnected waveguides.

B. Perfect splitting: interconnected rectangular waveguides

The proposed structure to enable perfect splitting of EM signals using interconnected rectangular waveguides

is shown in Fig. 2(a). Here we first focus on a four-port configuration; further examples using N interconnected waveguides are presented in the following sections. As observed in Fig. 2(a), the structure is composed of four outer waveguides, interconnected by four waveguides forming a junction (junction waveguides as defined in Sec. I). All the rectangular waveguides (outer and junction waveguides) are filled with a vacuum ($\mu_r = \varepsilon_r = 1$) and are surrounded by a perfect electric conductor (PEC). The width of the waveguides is chosen to be the same as in Ref. [45] to have the cutoff frequencies for the outer waveguides and the junction waveguides as $f_{c_w} \approx 1.043$ GHz and $f_{c_x} \approx 1.475$ GHz, respectively, with $f_{c_w} < f_{c_x}$. The widths of the outer and junction waveguides (direction perpendicular to the electric field) are given by $a_w = \lambda_{c_w}/2$ and $a_x = \lambda_{c_x}/2$, respectively, where w and x refer to the outer waveguides and the junction waveguides, respectively, and λ_c is the cutoff wavelength of the respective waveguide. The heights (in the direction parallel to the electric field) are given by $b_w = a_w/2$ and $b_x = a_x\Delta h$, respectively, initially with $\Delta h = 1/64$, again in line with Ref. [45]. The length of the outer waveguides is given by $\ell_w = 2a_w$ (an arbitrary value as waveguide ports will perfectly absorb the incoming waves), while the length of junction waveguides is given by $\ell_x = 1.2303\lambda_{c_x}$. It is important to note that this is the total length of the junction waveguides measured from outer waveguide to outer waveguide [see Fig. 2(a)]. As mentioned in Sec. I and

described below, perfect splitting in the proposed structure relies on an evanescent coupling between the outer waveguides and those at the junction. Because of this, the length l_x is a significant parameter that impacts the splitting ability of the structure. Larger values will reduce the evanescent field inside the junction, meaning that no perfect splitting will occur. A detailed discussion of this is provided later.

With this configuration, the proposed structure in Fig. 2(a) was numerically evaluated with use of the frequency-domain solver from CST Studio Suite®. To do this, four rectangular-waveguide ports were added to the outer waveguides. A tetrahedral mesh with adaptive refinement was implemented with a maximum cell density of 13 cells per wavelength inside and outside the model. Electric boundary conditions were set on all model boundaries to consider a PEC. For the regions that cannot touch the boundaries (e.g., around the junction waveguides as their dimensions are smaller than those of the outer waveguides) PEC was used as the background medium to ensure that all the waveguides are covered with PEC. Finally, the frequency-domain solver was configured with a third-order accuracy and the scattering parameters were calculated for a maximum of 100 001 frequency samples within the f/f_{c_x} range from approximately 0.67 to approximately 1.35.

The numerical results for the scattering parameters for the proposed four-port structure are presented in Figs. 2(b)(i)–2(b)(iv) for ports 1–4, respectively. The
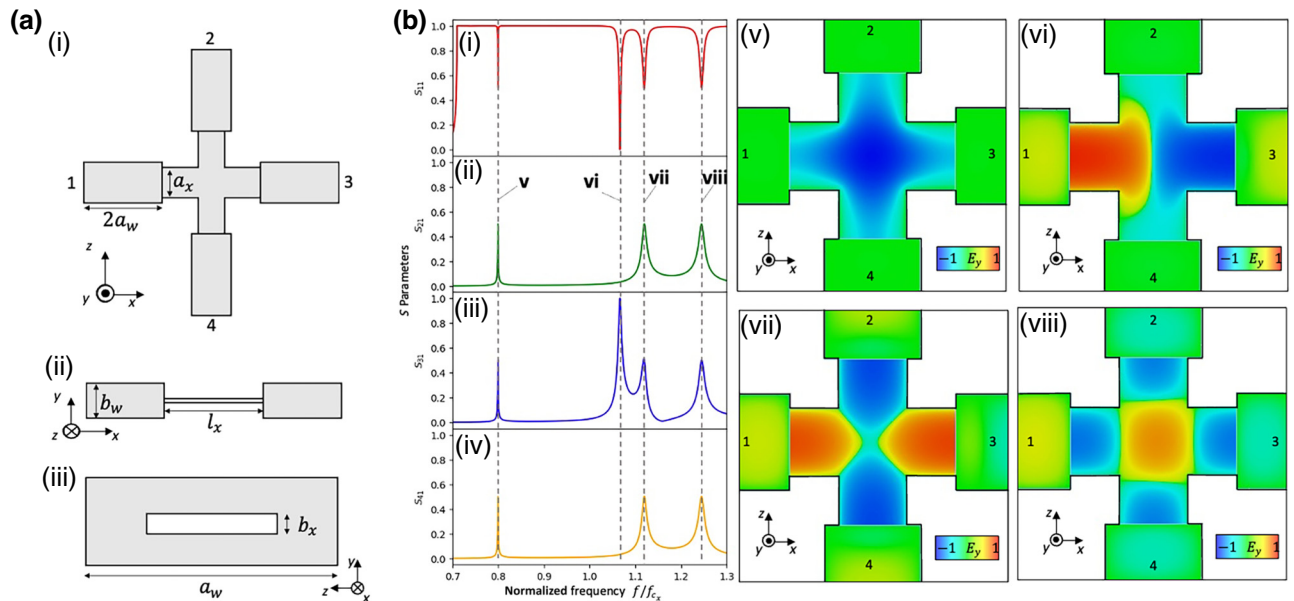

FIG. 2. Proposed idea for perfect splitting using interconnected rectangular waveguides: (a) (i)–(iii) Proposed structure (top, side, and front views, respectively) for perfect splitting of EM waves. The structure consists of outer waveguides with cutoff frequency $f_{c_w} \approx 1.043$ GHz (with height $b_w = a_w/2$ and width $a_w = 0.1016\sqrt{2}$) connected to a junction of waveguides having cutoff frequency $f_{c_x} \approx 1.475$ GHz (with height $b_x = a_w\Delta h$, width $a_x = a_w/\sqrt{2}$, and length $\ell_x \approx 1.2303\lambda_{c_x}$). (b) (i)–(iv) Scattering parameters for ports 1, 2, 3, and 4, respectively, for an input signal from port 1 calculated with CST Studio Suite®. (b) (v)–(viii) E_y distribution on the x-z plane (H plane) at each of the resonances shown in (i)–(iv) [see labels in panel (ii)].

scattering spectra have been normalized with respect to the cutoff frequency of the junction waveguides f_{c_x}, and the results are plotted for the normalized frequencies $0.7 \leq f/f_{c_x} \leq 1.3$ to account for incident frequencies above and below the cutoff frequency of the fundamental mode (TE_{10}) and higher-order mode (TE_{20}), respectively, of the outer waveguides. As observed, there are clear resonant frequencies where the amplitude at each port is approximately 0.5 (at normalized frequencies f/f_{c_x} of approximately 0.7967, approximately 1.1155, and approximately 1.2404), which is a condition for perfect splitting, as described in the previous section and in Eq. (1). Interestingly, there is a resonant frequency ($f/f_{c_x} = 1.0626$) where most of the incident signal is transmitted towards port 3, i.e., transmission of approximately 1 straight through. This latter resonance, while not used here for perfect splitting, may be attributed to the junction waveguides working as effective media emulating ε-near-zero metamaterials [45–50]. To further study the resonances shown in Figs. 2(b)(i)–2(b)(iv), the out-of-plane E_y distributions were extracted, and the results are shown in Figs. 2(b)(v)–2(b)(viii) [to guide the eye, see also labels v–viii in Fig. 2(b)(ii) for each resonant frequency]. As observed, the field distribution inside the junction waveguides resembles a line source along the out-of-plane direction for the first resonance [Fig. 2(b)(v)]. For the resonant frequencies where the amplitude of the transmitted and reflected signals is approximately 0.5 [Figs. 2(b)(v), 2(b)(vii), and 2(b)(viii)], the phase difference between the transmitted signal and the reflected signals is approximately π for the first and fourth resonances [Figs. 2(b)(v) and 2(b)(viii), respectively], with $\Delta\phi_{21}$ values of approximately 0.999π and approximately 1.006π, respectively, when it is calculated for port 2 and port 1. However, this is not the case for the third resonance [Fig. 2(b)(vii)], where a phase difference of approximately π is achieved only between port 2 and the rest of the ports (i.e., nonideal splitting). See Supplemental Material [44] for more details about the phase at each port for each of the resonances from Fig. 2. In this work, while the resonance appearing at a higher frequency [fourth resonance, Fig. 2(b)(viii)] also enables perfect splitting, we focus our attention on the first resonance [Fig. 2(b)(v)] as it appears at a lower frequency, enabling the implementation of a more-compact computing structure relative to the wavelength at the operational frequency. Notably, the first resonance that enables perfect splitting of EM signals appears at frequency $f_{c_w} < f < f_{c_x}$, (i.e., below the cutoff frequency of the junction waveguides), meaning that this resonance is the result of the coupling of an evanescent field to the junction waveguides. In the next section, we provide a theoretical analysis of the structure shown in Fig. 2(a) based on TL theory to understand how the reactive evanescent field can be modeled with equivalent-circuit models.

III. THEORETICAL ANALYSIS

In the previous section, it was shown how perfect splitting of EM signals can be achieved with interconnected rectangular waveguides as proposed in Fig. 2(a). This section focuses on the theoretical analysis of the proposed structure using TL theory, and the expansion of the structure to N ports. It is organized as follows: First, in Sec. III A, an equivalent two-port TL model for the structure shown in Fig. 2(a) is considered, where three of the four arms [here "arm" refers to an outer waveguide plus a junction waveguide connected at the junction, i.e., the device in Fig. 2(a) has a total of four arms] are grouped as an equivalent impedance. In this model, as shown later, an interface admittance and a junction admittance are considered to model the reactive fields at the interface between an outer waveguide and a junction waveguide and the reactive field at the junction between waveguides, respectively. The effect of these parallel admittances is discussed in detail in Sec. 4 in Supplemental Material [44]. Using this model, we present a fitting technique to calculate the parallel admittance modeling the reactive field at the junction waveguides. This is done by our combining a fitting algorithm with the TL model of the proposed structure. It is shown how such admittance can be calculated with use of a combination of numerical results (simulation) and analytical calculations via TL models and the *ABCD*-matrix method. In Sec. III B, it is shown how the proposed structure from Fig. 2(a) can be also used for perfect splitting using $N = 3$, 5, and 6 interconnected waveguides.

A. Effect of parallel interface and junction admittances: Equivalent-circuit model

The equivalent circuit for the proposed structure shown in Fig. 2(a) is presented in Fig. 3(a) and the desired response for this model is show in Fig. 3(b) (numerically calculated values). S'_{21} in Fig. 3(b) is given by $S'_{21} = \sqrt{S_{21}^2 + S_{31}^2 + S_{41}^2}$, where S'_{21} is the scattering parameter considering all the output ports. In the TL model shown in Fig. 3(a), the outer and junction waveguides (all filled with air, $\mu_r = \varepsilon_r = 1$) are modeled as TLs having impedance $Z_w = (\omega/\beta_w)(b_w/a_w)$ or $Z_x = (\omega/\beta_x)(b_x/a_x)$, respectively, propagation constant $\beta_w = k_0\sqrt{1 - (\pi/k_0 a_w)^2}$ or $\beta_x = k_0\sqrt{1 - (\pi/k_0 a_x)^2}$, respectively, and length ℓ_w or $\ell_x/2$, respectively, with ω the angular frequency and $k_0 = 2\pi f \sqrt{\mu_0 \varepsilon_0}$ the free-space wave number, where f is the incident frequency, ε_0 is the permittivity, and μ_0 is the permeability of free space. In the TL model, the length of each junction waveguide is considered to be $\ell_x/2$ to account for their length from the outer waveguides to the center of the junction [ℓ_x is measured from outer waveguide to outer waveguide, as described in Fig. 2(a)]. Finally, the time convention $e^{-i\omega t}$ is used. As mentioned in the previous section, ℓ_w can have an arbitrary

value as the outer waveguides are finished with absorbing ports in the numerical analysis; hence, in the TL model, they are simple impedances connected to the circuit [35]. The structure shown in Fig. 2(a) has two discontinuities where reactive fields can be considered [45]: (i) one at the interface between each of the outer waveguides and the junction waveguides [where the dimensions change from a_w to a_x along the z axis and from b_w to b_x along the y axis (considering the left waveguide)] and (ii) another at the center of the junction waveguides. To model the reactive fields at the interface between the outer and junction waveguides, one can place a parallel admittance between the two TLs modeling these waveguides. This is represented in Fig. 3(a), where a parallel admittance $Y_I = -i\Psi_I$ (interface admittance, with Ψ_I representing the coefficient

of the admittance) is placed between Z_w and Z_x for each of the four arms in the TL model. The nature of Y_I can be explained by considering the theory of waveguide discontinuities where a change of width and height at the interface between the waveguides can be modeled as an equivalent LC parallel circuit [38]. Similarly, a parallel admittance $Y_J = -i\Psi_J$ (junction admittance, with Ψ_J as the coefficient of the admittance) is also placed at the junction of the waveguides connecting the four arms to account for the reactive fields at the center of the junction, noting that such admittance could represent, for instance, a parallel capacitance [35,51].

To analyze the equivalent circuit from Fig. 3(a), for simplicity, the three output arms and Y_J from Fig. 3(a) (right panel) can be combined into a single impedance Z_{tot_1}
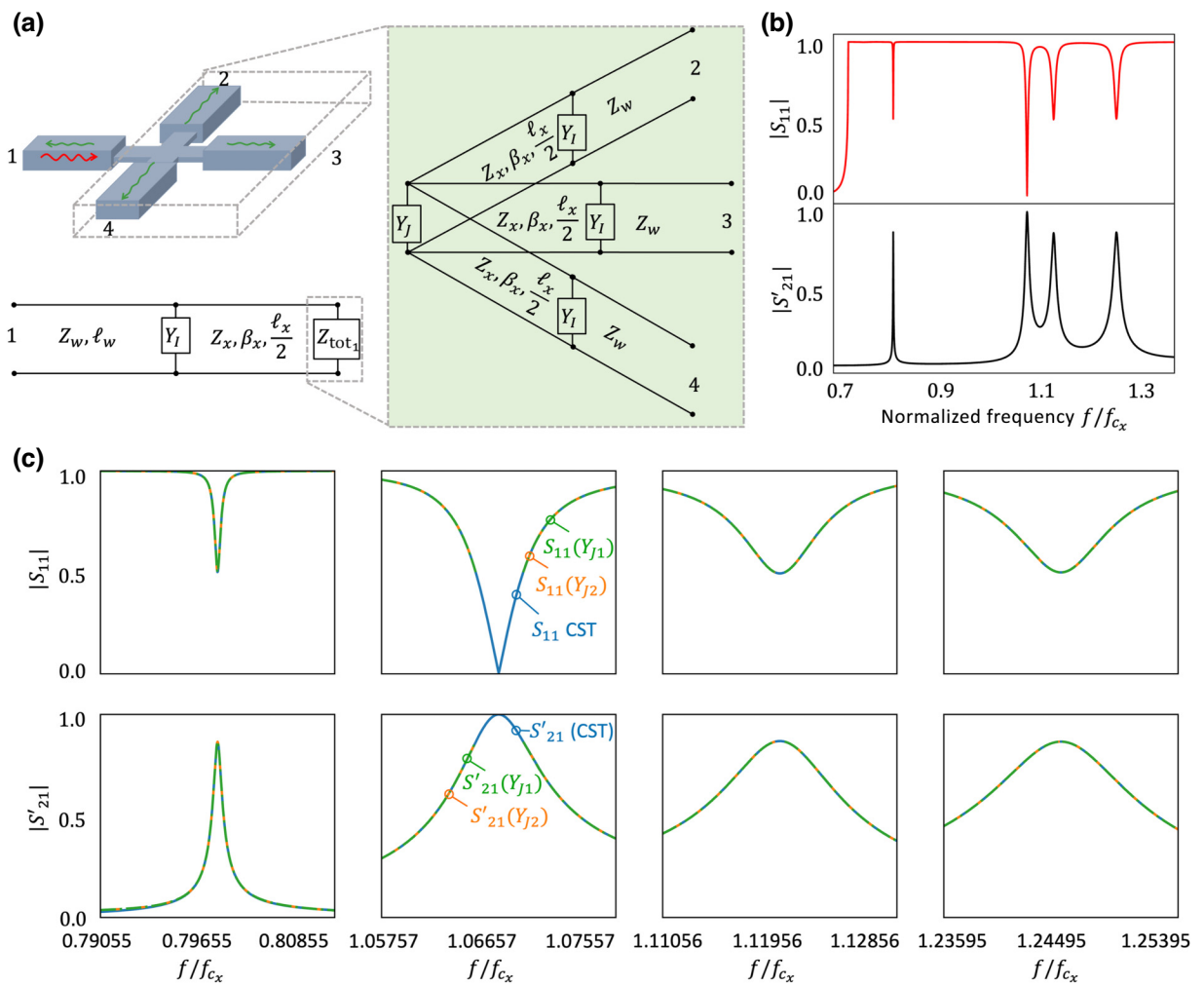

FIG. 3.   TL model of the proposed four-port waveguide junction for perfect splitting: lumped-element representation of output arms. (a) A four-port perfect splitter [same structure as in Fig. 2(a)] and an equivalent TL model, consisting of three arms (highlighted in the green box) with outer-waveguide impedance Z_w, outer-waveguide length ℓ_w, interface admittance Y_I, junction-waveguide impedance Z_x, propagation constant β_x and junction-waveguide length $\ell_x/2$. The arms are connected to a parallel admittance Y_J. (b) Numerical results for the scattering spectra, S_{11} (top) and S'_{21} (bottom), calculated with CST Studio Suite®. (c) Scattering parameters [$|S_{11}|$ (top row) and $|S'_{21}|$ (bottom row)] for a narrow frequency window around each resonance calculated numerically (blue) and theoretically (dashed orange and green lines).

[see the schematic representation in the bottom panel in Fig. 3(a)] as follows [35]:

$$Z_{\text{tot}_1} = \left(Y_J + \frac{3}{Z_{\text{in}}}\right)^{-1}, \tag{2}$$

where Z_{in} is the input impedance seen from the center of the junction towards an output port. From TL theory, Z_{in} can be expressed as [44]

$$Z_{\text{in}} = Z_x \frac{Z_{\text{par}_1} - iZ_x \cos(\beta_x \ell_x/2)}{Z_x - iZ_{\text{par}_1} \cos(\beta_x \ell_x/2)}, \tag{3}$$

with $Z_{\text{par}_1} = (Y_I + (1/Z_w))^{-1}$. With these simplifications, the resulting circuit model is reduced to [see the bottom panel in Fig. 3(a)] an input arm (consisting of a TL modeling the single outer waveguide connected to port 1, a parallel admittance representing the interface between the outer waveguide and the junction waveguide Y_I, and a TL representing the junction waveguide for this arm) connected to the load impedance, Z_{tot_1}. To extract the scattering parameters of this simplified two-port TL circuit, the *ABCD*-matrix method is used [35]. On the basis of this, the TL representing the junction waveguide of the input arm and the interface admittance Y_I from the bottom panel in Fig. 3(a) can be defined by the following 2×2 matrices [35]:

$$ABCD_x = \begin{bmatrix} \cos(\beta_x l_x/2) & -iZ_x \sin(\beta_x l_x/2) \\ -i\frac{1}{Z_x} \sin(\beta_x l_x/2) & \cos(\beta_x l_x/2) \end{bmatrix}, \tag{4a}$$

$$ABCD_{Y_I} = \begin{bmatrix} 1 & 0 \\ Y_I & 1 \end{bmatrix}. \tag{4b}$$

An overall total *ABCD* matrix defining the circuit in Fig. 3(a) (bottom panel) can then be obtained by simply multiplying the two matrices described above. i.e., $ABCD_{\text{eq}} = ABCD_{Y_I} \cdot ABCD_x$. The scattering parameters for the reflection and transmission coefficients, S_{11} and S_{21}, for the two-port equivalent circuit in Fig. 3(a) (bottom panel) can then be calculated as [52]

$$S_{11} = \frac{A_{\text{eq}} Z_{\text{tot}_1} + B_{\text{eq}} - C_{\text{eq}} \overline{Z_w} Z_{\text{tot}_1} - D_{\text{eq}} \overline{Z_w}}{A_{\text{eq}} Z_{\text{tot}_1} + B_{\text{eq}} + C_{\text{eq}} Z_w Z_{\text{tot}_1} + D_{\text{eq}} Z_w}, \tag{5a}$$

$$S_{21} = \frac{2\sqrt{\text{Re}\{Z_w\}\text{Re}\{Z_{\text{tot}_1}\}}}{A_{\text{eq}} Z_{\text{tot}_1} + B_{\text{eq}} + C_{\text{eq}} Z_w Z_{\text{tot}_1} + D_{\text{eq}} Z_w}, \tag{5b}$$

where $\overline{Z_w}$ denotes the complex conjugate operator, $A_{\text{eq}}, B_{\text{eq}}, C_{\text{eq}},$ and D_{eq} are the components of the $ABCD_{\text{eq}}$ matrix, and Re{ } denotes the real component [45].

Once a circuit model has been defined, the main challenges are now to calculate Y_I and Y_J and to understand how they affect the overall response of the equivalent circuit. Results for the influence of these two admittances

are presented in Fig. S3 in Supplemental Material [44], showing that varying the value of Y_I has a negligible effect on enabling the model to accurately represent the structure; therefore, we focus our efforts on calculating Y_J. Moreover, as shown in Fig. S3(c), a constant value of admittance enables the TL model to match only the first peak from the numerical results, as expected, indicating that a frequency-dependent $\Psi_J(f/f_{c_x})$ [i.e., $Y_J(f/f_{c_x})$] is necessary to model the full spectral response of the proposed structure. Because of the complexity of the calculation of the frequency-dependent admittance via closed-form solutions, we developed an algorithm that uses the TL model from Fig. 3(a) and allows us to calculate the admittance within the frequency range under study by considering the numerically calculated transmission and reflection spectra, i.e., a quasianalytical or inversion-based fitting technique [35,53]. From these results, agreement between the numerical and theoretical values for $|S'_{21}|$ is expected. As shown in Fig. 3(c), the theoretical results for $|S_{11}|$ fit the numerical results well for all resonances except the second resonance, where there is a missing set of values that extend below $|S_{11}| = 0.5$. For the transmitted spectra towards port 2, $|S_{21}|$, the numerical results for the first resonance reach $|S_{21}| = 0.5$ at the resonant frequency, the condition for perfect splitting [as shown in Fig. 2(b)]. With the lumped-element representation [shown in Fig. 3(a)], we should expect a perfect-splitting transmission of $|S'_{21}| = \sqrt{0.75} \approx 0.8660$ because all output ports have now been combined into a single parallel impedance. Similarly, the value of $|S'_{21}|$ from the numerical solutions should also agree with this value. This can be seen in Fig. 3(b), where $|S'_{21}|$ has a value of 0.8655 for the first resonance, for instance. With our theoretical approach, the analytically calculated values of $|S'_{21}|$ for the three resonances shown in Fig. 3(c) (first, third, and fourth columns) are 0.8657, 0.8660, and 0.8660, respectively, with all three values demonstrating a close fit to the numerical solutions [also shown in Fig. 3(c)]. However, because of the unequal splitting nature of the second resonance (where straight-through transmission of approximately 1 is obtained, as discussed in Fig. 2), a different circuit model would be required to fit the transmission spectrum around this resonance. This could be done, for instance, by one considering series impedances (one per arm) connected to the junction parallel admittance Y_J. In this context, each of these series impedances could be different to account for nonequal splitting between all the arms. However, this is beyond the scope of the present work as our aim is to use the proposed structure for perfect splitting of EM signals. As discussed, this method of implementing a conic section enables us to calculate values of Y_J (or its coefficient Ψ_J) that satisfy the numerically calculated scattering parameters. However, as this is done with only the perfect-splitting magnitude requirement, one cannot assume that the phase condition for perfect splitting will also be satisfied. In Supplemental

Material [44], we explore an alternative technique to retrieve Y_J for the first resonant frequency where the perfect splitting constraints are directly taken into account, such as the phase difference between output and input ports and voltages at each port.

B. Perfect splitting: *N*-port configurations

The previous sections focused on the study of the structure in Fig. 2(a) using a four-port configuration of interconnected rectangular waveguides for perfect splitting. The aim in this subsection is to demonstrate how the proposed structure can also be used for an arbitrary number of ports N. To do this, one should consider the following: (i) As discussed in Figs. 1–3, an incident signal applied from an input port will *see* a different impedance at the center of the junction waveguides, an impedance that will depend on the number of arms $N-1$ connected to the junction (see Fig. 1). Because of this, it would be expected that if N is changed, the resonant frequency at which the perfect splitting occurs will also shift. (ii) Moreover, the role of the dimensions of the cross section and the length of the outer waveguides and the junction waveguides should also

be taken into account as, for instance, the latter waveguides will limit the number of arms that one can connect at the center. Initial numerical studies were performed with the structure in Fig. 2(a) for three-, four-, and five-port configurations. From this, an increase in the number of ports caused a redshifted perfect-splitting frequency (i.e., a shift towards the cutoff frequency of the outer waveguides f_{c_w}, not shown). On the basis of this, to be able to increase the number of arms (and hence ports) connected at the junction and to prevent the perfect-splitting frequency from falling below f_{c_w} (which would prevent perfect splitting from occurring as all outer and junction waveguides would be operating below the cutoff frequency of their fundamental mode), in this subsection both the outer-waveguide and the junction-waveguide cutoff frequencies are modified to $f_{c_w} = 1.0$ GHz and $f_{c_x} = 1.8$ GHz, respectively. As observed, f_{c_x} has now been increased compared with the frequency for the structure discussed in Figs. 1–3; this is to enable the redshifting of the perfect-splitting frequency when N is increased to be greater than f_{c_w} and less than f_{c_x}, as mentioned before, without excitation of higher-order modes in the outer waveguide (i.e., $f_{c_x} < 2f_{c_w}$ in our case).
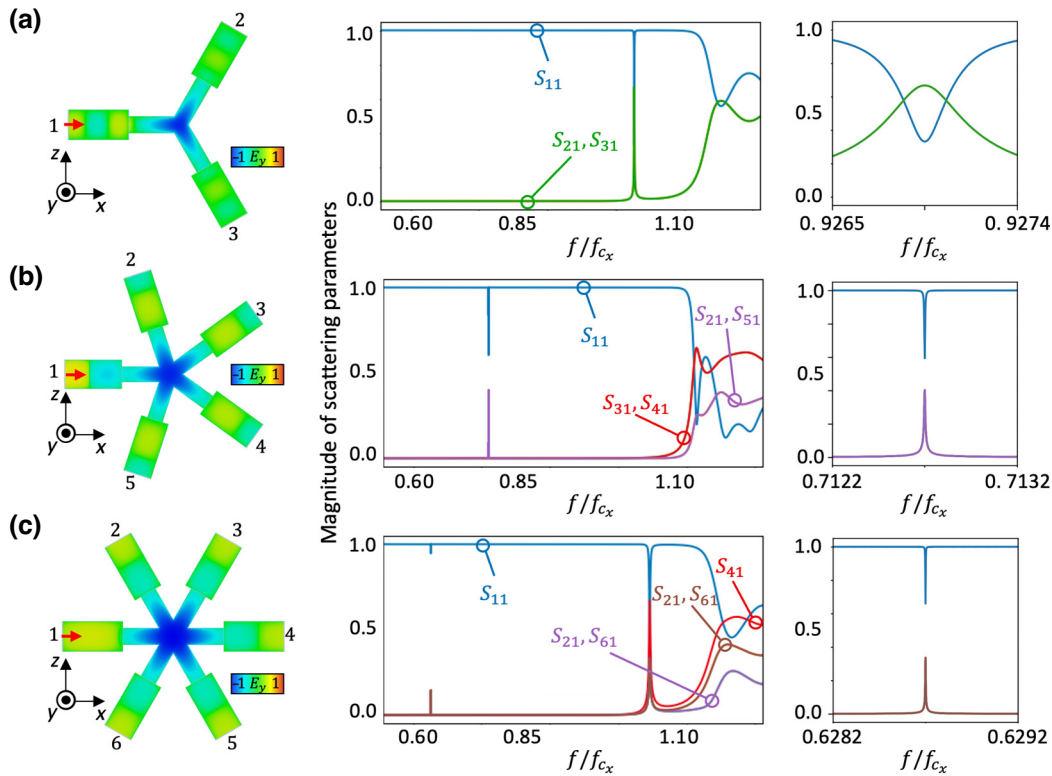

FIG. 4. Perfect splitting with N-port interconnected rectangular waveguides. (a)–(c) Left: E_y distribution on the x-z plane (H plane) for the three-, five-, and six-port structures, respectively. Middle: Scattering parameters for the full spectral window. Right: Scattering parameters for a narrow frequency range around each perfect-splitting resonance from the middle plot. The reflection (towards port 1) and transmission (towards each of the output ports, ports 2 to N) coefficients $|\rho|$ and $|\gamma|$ for the three-, five-, and six-port structures are 0.3313 and 0.6669, respectively, 0.5929 and 0.4025, respectively, and 0.6599 and 0.3357 respectively. These results are in good agreement with the expected values of perfect splitting in ideal TLs as discussed in Sec. II A with $|\rho| = |(2-N)N^{-1}|$ and $|\gamma| = |2N^{-1}|$.

Next, we can consider the length of the junction waveguides as a key parameter to be able to physically fit an increased number of arms connected to the junction. As the frequency at which perfect splitting occurs will be less than f_{c_x}, it is the evanescent field inside the junction waveguides (working below their cutoff frequency f_{c_x}) that enables perfect splitting. Extending the length ℓ_x will reduce the evanescent field that reaches the center of the junction waveguides, meaning that this length should be carefully chosen such that evanescent coupling to the junction still exists. A detailed numerical study of the influence of the length and height of the cross section of the hollow for the junction waveguides (dimensions ℓ_x and $b_x = a_x \Delta h$, respectively) is presented in Supplemental Material [44], where the results of a parameter sweep of the height for two junction lengths of the channel are shown. From those results, increasing ℓ_x causes the response of the structure to be more narrowband, a response that can be overcome by, for instance, increasing Δh (see also Appendix A, where the spectral response when ℓ_x is modified for a fixed Δh is presented). Interestingly, this means that narrow hollow waveguides are not required in our case to enable perfect splitting of EM signals. From now on, to evaluate the perfect-splitting response using N-port structures and to apply them for computing processes in the next section, the dimensions $\ell_x = 3\lambda_{c_x}$ and $\Delta h = 0.5$ are used, with waveguide cross sections modified as explained above in this section.

The numerical results for the out-of-plane E_y distribution obtained for the proposed interconnected rectangular waveguides for $N = 3$, 5, and 6 arms are shown on the left panels in Figs. 4(a)–(c). These results are calculated at the frequency where perfect splitting occurs for each value of N, respectively. As observed, the field distributions resemble the one shown for $N = 4$ in Fig. 2, as expected. Scattering parameters for each of the N ports are presented in the middle in Figs. 4(a)–(c), with additional enlarged plots around the perfect-splitting resonance shown on the right panels in Figs. 4(a)–(c). As expected, the perfect-splitting frequency is redshifted when N is increased, as discussed above. Moreover, the splitting ratios ($|S_{11}|/|S_{N1}|$) for the structures with $N = 3$, 5, and 6 are approximately 1:2, approximately 3:2, and approximately 2:1, respectively (see the exact values in the caption for Fig. 4). These results are in agreement with the theoretical values from Eq. (1), demonstrating how perfect splitting can be achieved with the proposed structure for N ports. As shown in Fig. 4, here we have considered $N = 6$ as the maximum value. This could be increased by, for instance, carefully increasing the length of the junction waveguides to fit more arms while ensuring that the coupled evanescent field still reaches the junction. However, increasing N will redshift even more the perfect-splitting resonance, meaning that the dimensions of the outer-waveguide and junction-waveguide cross sections may need to be

modified (this is beyond the scope of the present work). The proposed structure for perfect splitting of EM signals is used in the next section for fundamental computing processes, including routing of information.

IV. USE OF PERFECT SPLITTING FOR COMPUTING: EXAMPLES

In the previous sections, perfect splitting of EM signals was achieved with interconnected rectangular waveguides. Here it is shown how this performance can be used in fundamental computing operations such as routing of information and linear comparators. We recently showed how such operations can be performed with arrays of parallel-plate waveguides as ideal TLs [34,36]. Here we demonstrate that it is also possible to use rectangular waveguides, which are technologically important devices. Interestingly, while here we focus on two fundamental computing processes, perfect splitting of EM signals has been shown to be an interesting mechanism to design, for instance, photonic structures to calculate temporal derivatives or the solution of partial differential equations [20,39,41,54]. We envision that our proposed structures from the previous sections could also be used in this realm, a study that is currently under development and that will be presented elsewhere.

A. Routing of EM signals

For this scenario, a four-port ($N = 4$) configuration of interconnected rectangular waveguides is used [as discussed in Fig. 2(a)]. The dimensions of the outer and junction waveguides are the same as those shown in Fig. 4 (for $f_{c_w} = 1.0$ GHz and $f_{c_x} = 1.8$ GHz). To enable routing of information from one port to another port, we make use of the linear interaction between two incident signals applied from two different ports. Different scenarios considering input signals from ports 1 and 2 and from ports 1 and 3 are shown in Figs. 5(a) and 5(b) and Figs. 5(c) and 5(d), respectively, with use of different phases between the two incident signals.

We first focus on the case shown in Fig. 5(a), where two incident signals are applied (one from port 1 and one from port 2). These two signals are in phase, as represented in Fig. 5(a)(i) as solid red and blue waves, respectively. When we are working at the perfect-splitting resonance, as described in the previous sections, each incident signal will split into four signals (eight in total). Each of the new generated signals is depicted as a dashed line in Fig. 5(a)(i). All these scattered waves will have the same magnitude, with a phase difference between the transmitted and reflected signals of π. The final output will simply be defined by Eq. (1), i.e., the signals traveling towards ports 1–4 after both incident signals have passed the junction will be the linear superposition of all the scattered signals. As a result, some signals will constructively or destructively interfere due to being in phase or out of
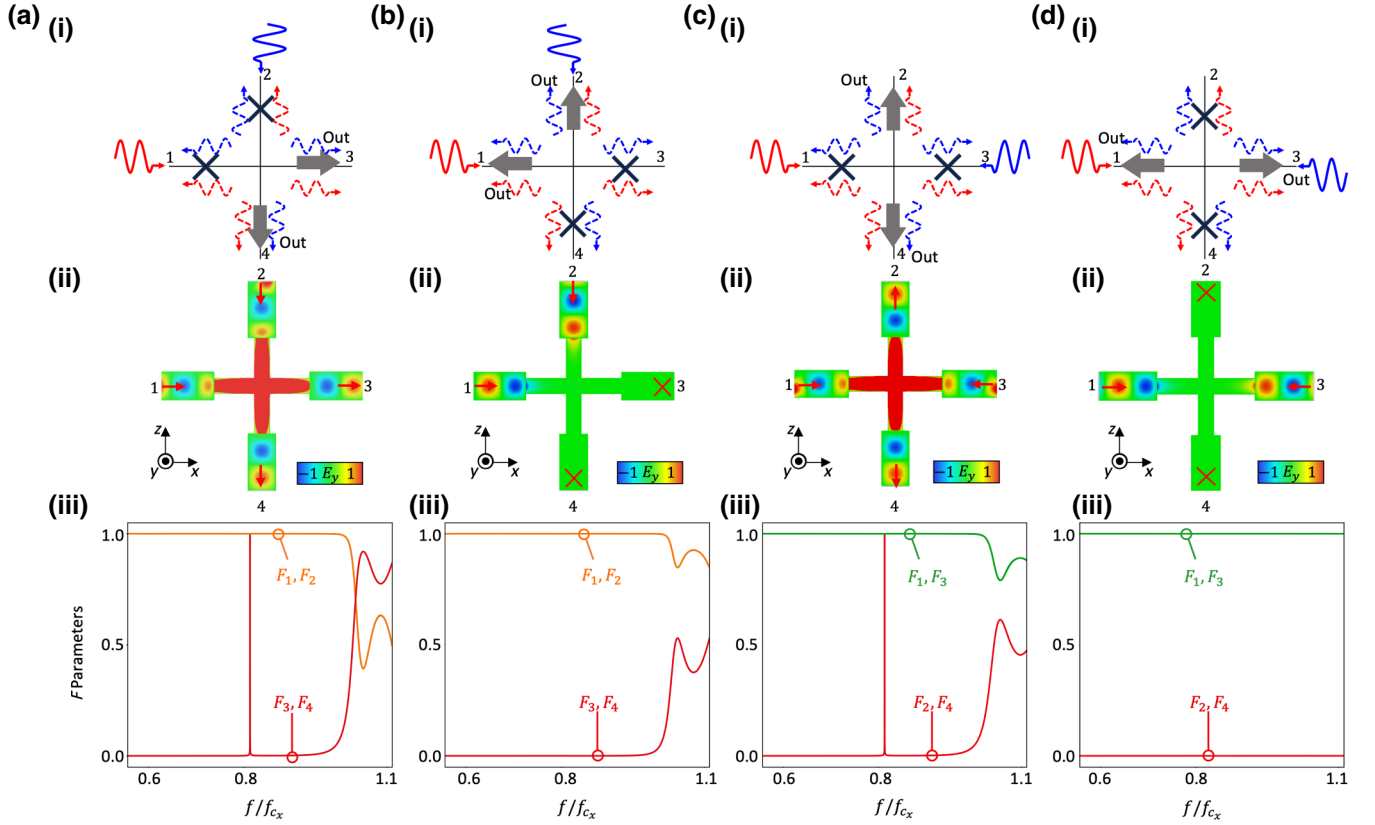
FIG. 5. Demonstration of routing of information using a four-port interconnected-rectangular-waveguide structure. (a),(b) Input signals from ports 1 and 2 and (c),(d) input signals at ports 1 and 3 for the in-phase condition and the out-of-phase condition, respectively. (i) The resulting interference of all the scattered signals generated after the input signals are perfectly split when passing the junction. (ii) E_y distribution on the x-z plane (H plane). (iii) F parameters for the full spectral window, for each respective input and phase combination. For completeness, see Appendix B for the full analytical values at the output ports for inputs from ports 1 and 2 with different phase difference between the incident signals.

phase. This is schematically shown in Fig. 5(a)(i). As observed, no output signals traveling towards ports 1 and 2 are obtained, while clear output signals exist traveling towards ports 3 and 4. This behavior is also demonstrated in Fig. 5(a)(ii), where the numerical results for the E_y distribution are presented at the perfect-splitting resonant frequency. Finally, the combined scattering parameters for two input signals (i.e., the F parameters, representing the output spectra at a port when the two incident signals are considered as a simultaneous excitation [55,56]) are presented in Fig. 5(a)(iii), where it can be seen how full transmission (value of approximately 1) is obtained at ports 3 and 4 when working at the first resonance ($f/f_{c_x} \approx 0.8125$). To verify these results, one can apply Eq. (1) with an input vector of signals $\mathbf{x} = [1, 1, 0, 0]$, resulting in the following output vector of signals $\mathbf{y}$:

$$\mathbf{y} = \begin{bmatrix} -0.5 & 0.5 & 0.5 & 0.5 \\ 0.5 & -0.5 & 0.5 & 0.5 \\ 0.5 & 0.5 & -0.5 & 0.5 \\ 0.5 & 0.5 & 0.5 & -0.5 \end{bmatrix} \begin{bmatrix} 1 \\ 1 \\ 0 \\ 0 \end{bmatrix} = \begin{bmatrix} 0 \\ 0 \\ 1 \\ 1 \end{bmatrix}, \quad (6)$$

which is in agreement with the values from Fig. 5(a)(iii). Conversely, consider now two input signals applied from ports 1 and 2 with a phase difference of π, $\mathbf{x} = [1, -1, 0, 0]$. This scenario is schematically shown in Fig. 5(b). Following the same process as in Fig. 5(a)(i), the final signal transmitted towards each of the ports will be the linear superposition of all the scattered signals produced by each of the applied inputs. In this way, the two signals scattered towards ports 3 and 4 are out of phase, while the signals scattered towards ports 1 and 2 are in phase. As a result, output signals are observed only at ports 1 and 2. This is again in line with Eq. (1), which predicts an output vector of signals $\mathbf{y} = [-1, 1, 0, 0]^T$. The numerical results for this case are shown in Figs. 5(b)(ii) and 5(b)(iii) for the E_y distribution at the perfect-splitting frequency and the full spectral response of the F parameters, respectively. Further examples are shown in Figs. 5(c) and 5(d) for input signals applied from ports 1 and 3 being in phase or out of phase, respectively. For these two cases, in-phase input signals [Fig. 5(c)] $\mathbf{x} = [1, 0, 1, 0]$ and out-of-phase input signals [Fig. 5(d)] $\mathbf{x} = [1, 0, -1, 0]$, the output

vector of signals is $\mathbf{y} = [0, 1, 0, 1]^T$ and $\mathbf{y} = [-1, 0, 1, 0]^T$, respectively, after use of Eq. (1). These results are again in agreement with numerical calculations, as shown in Figs. 5(c)(ii) and 5(c)(iii) and Figs. 5(d)(ii) and 5(d)(iii), respectively.

B. Linear comparator

An interesting application of perfect splitting is that it can be used to perform the comparison between the amplitudes of two inputs [36]. Here we demonstrate that such computing operation can also be achieved with the proposed perfect splitters via interconnected rectangular waveguides. This amplitude-comparison operation is performed by use of the phase interaction in a three-port perfect-splitting structure. Consider an $N = 3$ interconnected-rectangular-waveguide junction where ports 1 and 2 are used as inputs, while port 3 is

considered an output port. The amplitude and phase of the incident and output signals at each port are $a_1^{i/o}$ and $\phi_1^{i/o}$, $a_2^{i/o}$ and $\phi_2^{i/o}$, and $a_3^{i/o}$ and $\phi_3^{i/o}$, respectively, with superscripts i and o representing "input" and "output", respectively. If the signals from ports 1 and 2 are simultaneously applied to the structure with $a_1^i = a_2^i$ but different phases such that $\phi_1^i - \phi_2^i = \pi$, and following Eq. (1), ports 1 and 2 will see a reflected signal of opposite phase (or polarity), while port 3 will see no signal. Such performance can then be exploited to compare the amplitude of two incident signals. Note that a phase difference of π between the incident signals is necessary to facilitate destructive interference between them, enabling the output phase to be dominated by the phase of the larger incident signal (see Appendix C for the effect of using different phases of the input signals). As shown in Ref. [36] using ideal parallel-plate waveguides, a comparator operation
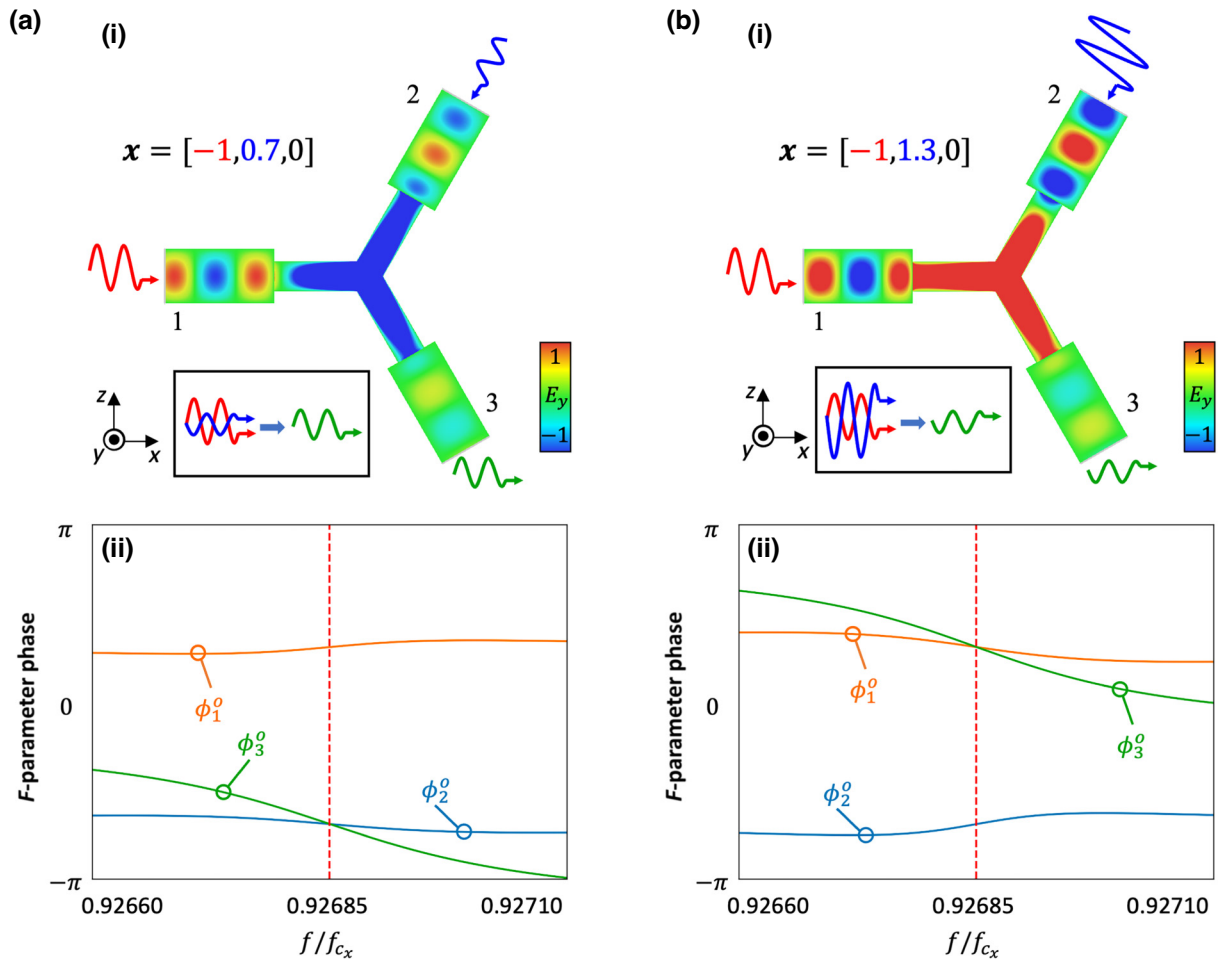

FIG. 6. Demonstration of a $N = 3$ interconnected-rectangular-waveguide-junction amplitude comparator. (a) Case 1, $a_1^i > a_2^i$. (b) Case 2, $a_1^i < a_2^i$. (i) E_y distribution on the x-z plane (H plane) at the resonant frequency shown as a vertical dashed line in (ii). The signals shown as insets represent how the scatterings produced by the two incident signals interact. This enables a comparison operation through their superposition when they are propagating along the third waveguide (output waveguide, green signal). (ii) F-parameter phase for a narrow spectral window around the first resonance where perfect splitting occurs ($f/f_{c_x} \approx 0.9269$).

can be done by one considering two square pulses with opposite polarities applied to ports 1 and 2 in an $N=3$ network of ideal waveguides. Then one can look at the phase (polarity) of the output pulse towards port 3 and determine which input pulse had the largest amplitude. A demonstration of this scenario using our approach is shown in Fig. 6. First, we can consider the two incident signals defined by the input vector $\mathbf{x} = [-1, 0.7, 0]$ (noting that both incident signals have different amplitude and opposite phase). Following Eq. (1), the output vector of signals is as follows:

$$\mathbf{y} = \begin{bmatrix} -1/3 & 2/3 & 2/3 \\ 2/3 & -1/3 & 2/3 \\ 2/3 & 2/3 & -1/3 \end{bmatrix} \begin{bmatrix} -1 \\ 0.7 \\ 0 \end{bmatrix} = \begin{bmatrix} 0.8 \\ -0.9 \\ -0.2 \end{bmatrix}, \quad (7)$$

which demonstrates that the phase of the output signal at port 3 is dominated by the phase of the input signal at port 1 (the larger-amplitude input) since both values are negative. These results are in agreement with Fig. 6(a)(i), where the E_y distribution on the x-z plane is plotted. As observed, the phase of the output signal at port 3 is the same as the phase of the output signal at port 2 but opposite that of the output signal at port 1, in agreement with Eq. (7).

For completeness, the output-signal phase spectra are shown in Fig. 6(a)(ii), where it is also seen how the phases are in agreement with Eq. (7). Finally, the opposite condition is also demonstrated in Fig. 6(b), where now the amplitude of the incident signal from port 2 is larger than that from port 1. Here $\mathbf{x} = [-1, 1.3, 0]$, resulting in an output vector $\mathbf{y} = [1.2, -1.1, 0.2]^T$ from Eq. (1). Note that now the phase (polarity) of the signal at port 3 is the same as the phase of the input signal from port 2, which is the opposite of what happened in the example in Fig. 6(a), corroborating that now the incident signal from port 2 has higher amplitude than the incident signal from port 1.

The corresponding numerical results for the E_y distribution at the resonant frequency along with the F-parameter phase are shown in Figs. 6(b)(i) and 6(b)(ii), respectively, demonstrating good agreement with the theoretical values. The results presented here may also be scaled to higher frequencies such as the optical regime via plasmonic waveguides modeled via TL and equivalent-circuit techniques [57,58].

V. CONCLUSION

A structure to achieve perfect splitting of EM waves has been proposed and evaluated both theoretically and numerically. The proposed structure consists of N interconnected rectangular waveguides. It was demonstrated that perfect splitting cannot occur when one considers just the junction of waveguides given that their width (in the direction perpendicular to the electric field) is on the order of the wavelength at the operational frequency. To tackle this, additional outer waveguides, with a cutoff frequency below that of the junction waveguides, were considered. Thus, it was shown that it is possible to achieve perfect splitting of EM waves when working below the cutoff frequency of the junction waveguides, i.e., there is an evanescent field coupled to the junction waveguides, exciting a junction resonance. The proposed structure was then evaluated theoretically with use of TL models, and it was demonstrated how the evanescent coupling and junction resonant frequency can be approximately modeled via parallel admittances in the equivalent circuit. Different scenarios of perfect splitting were demonstrated, including $N=3$, 4, 5, and 6 interconnected waveguides, showing excellent agreement with the theory of perfect splitters. Finally, the proposed structure was used to perform fundamental computing operations, such as routing of information and comparison operations. We envision
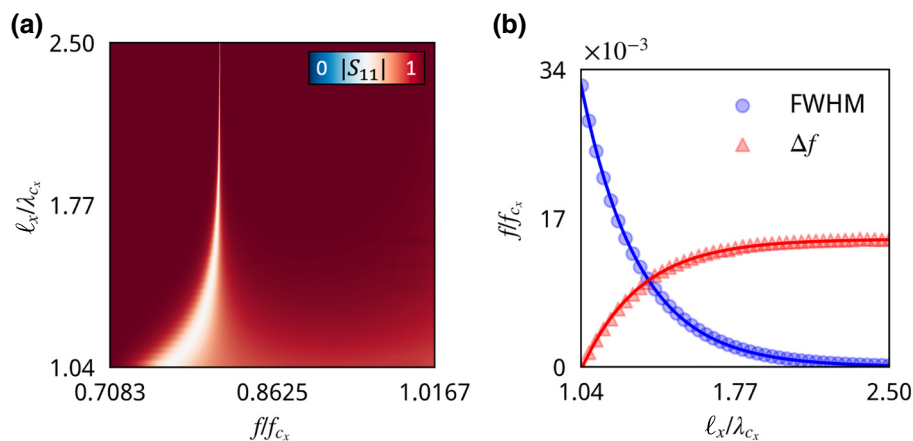

FIG. 7. (a) Numerical results for S_{11} as a function of f/f_{c_x} and ℓ_x/λ_{c_x}. (b) FWHM (blue) and frequency shift Δf (red). Δf represents the change in center frequency of the first resonance from its frequency at $\ell_x/\lambda_{c_x} = 1.04$. These parameters were obtained by our considering the waveguide cross sections as those in Fig. 2(a).
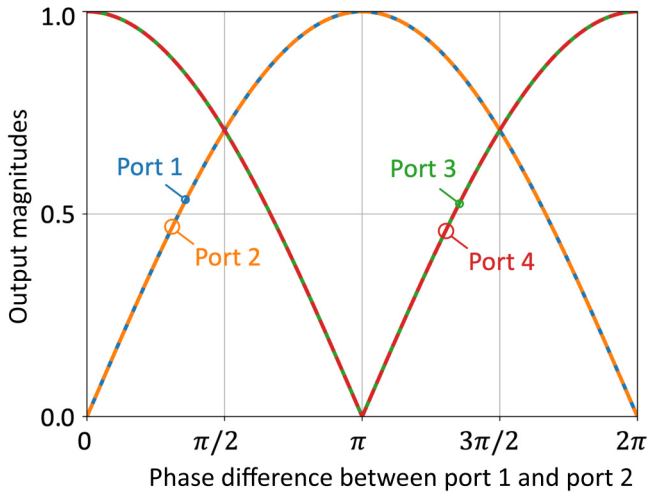
FIG. 8.   Full output of a four-port perfect splitter with two inputs of equal magnitude at port 1 and port 2 when the input phase is varied analytically calculated with the perfect-splitter scattering matrix defined in Eq. (1) and input vector $\mathbf{x} = [1, 1e^{i\phi}, 0, 0]$, where ϕ is the phase difference between port 2 and port 1, with the phase of the signal at the latter port as zero (used as a reference).

that the proposed mechanism for perfect splitting of EM waves could be implemented in large networks to perform, for instance, the solution of partial differential equations of derivatives in both the time domain and the frequency domain, opening up further opportunities for computing with waves.

The datasets generated and analyzed during the current study are available from the corresponding author upon reasonable request.

APPENDIX A

The effect of changing the dimension ℓ_x using a four-port junction of rectangular waveguides as proposed in Fig. 2(a) is shown in Fig. 7, where a contour plot of the reflection spectra as a function of ℓ_x for the first resonant frequency is presented. Figure 7 shows the effect of increasing the channel length on the FWHM and the position of the first resonance. Larger values of ℓ_x will reduce the evanescent field coupled to the junction waveguides, meaning that perfect splitting will eventually disappear.

APPENDIX B

In Fig. 5 it is shown how routing of information can be achieved with a four-port interconnected-rectangular-waveguide structure when two ports are excited either in phase or out of phase. For completeness, Fig. 8 presents the full set of output signals theoretically calculated with Eq. (1) for ideal interconnected transmission lines.

APPENDIX C

In Sec. IV B, a phase difference of π between the input signals is used, the reasoning behind this is that with a phase difference of π, the phase of the output signal is equals to the phase of the input signal with larger
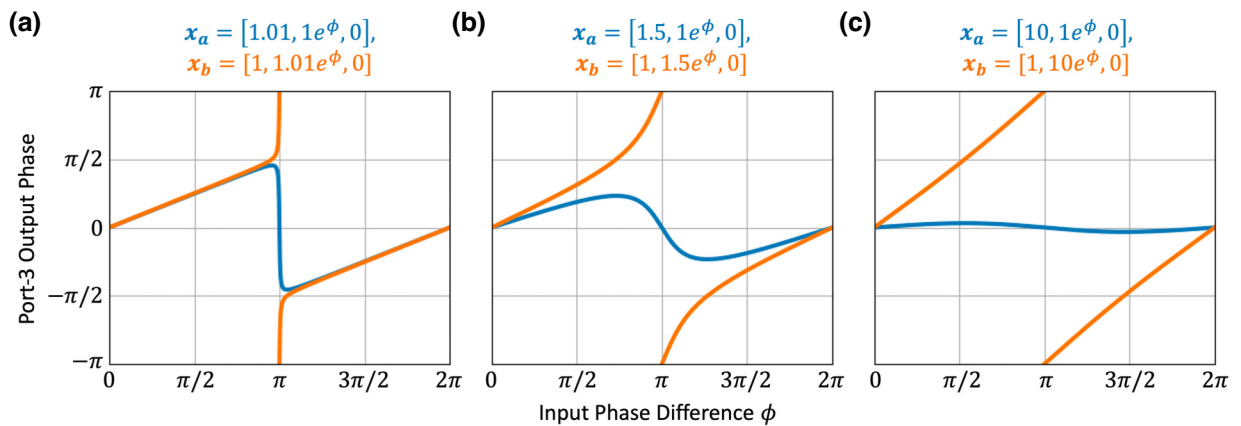

FIG. 9.   Output phases of a three-port perfect splitter for two input cases $\mathbf{x}_a$ and $\mathbf{x}_b$. Phase of the signal at the output port (port 3) for three different input magnitude ratios—(a) 1.01:1, (b) 1.5:1, and (c) 10:1—for the cases where the magnitudes of port 1 (|port 1|) and port 2 (|port 2|) are: |port 1|>|port 2| (blue lines) and |port 1|<|port 2| (orange lines).

magnitude. However, diverging from this condition, the output phase is not equal to the phase of either input signal. This is highlighted in Fig. 9. When the magnitude of the two input signals are almost equal, it can be seen that the output phase diverges from either input phase as the phase difference diverges from π. Comparatively, as we increase the difference between the magnitudes of the incident signals in Figs. 9(b) and 9(c), the output phase is close to the phase of the larger input signal. However, the output phase is only exactly equal to the phase of the larger magnitude when the input phase difference is π.

———————

[1] T. N. Theis and H.-S. P. Wong, The end of Moore's law: A new beginning for information technology, Comput. Sci. Eng. **19**, 41 (2017).

[2] P. A. Gargini, F. Balestra, and Y. Hayashi, The International Roadmap for Devices and Systems: A beacon for the electronics industry, Computer **55**, 4 (2022).

[3] C. E. Leiserson, N. C. Thompson, J. S. Emer, B. C. Kuszmaul, B. W. Lampson, D. Sanchez, *et al.*, There's plenty of room at the top: What will drive computer performance after Moore's law?, Science **368**, 1 (2020).

[4] K. R. Gauen, *The effects of MOSFET output capacitance in high frequency applications* (IEEE, San Diego, 1989), Vol. 2, pp. 1227–1234, https://api.semanticscholar.org/CorpusID:15969223.

[5] A. Steane, Quantum computing, Rep. Prog. Phys. **61**, 117 (1998).

[6] S. Regot, J. MacIa, N. Conde, K. Furukawa, J. Kjellén, T. Peeters, *et al.*, Distributed biological computation with multicellular engineered networks, Nature **469**, 207 (2011).

[7] K. P. Kalinin, G. Mourgias-Alexandris, H. Ballani, N. G. Berloff, J. H. Clegg, D. Cletheroe, *et al.*, Analog iterative machine (AIM): using light to solve quadratic optimization problems with mixed variables, arXiv:230412594 (2023).

[8] T. Knightley, A. Yakovlev, and V. Pacheco-Peña, Neural network design of multilayer metamaterial for temporal differentiation, Adv. Opt. Mater. **11**, 2202351 (2023).

[9] N. M. Estakhri, B. Edwards, and N. Engheta, Inverse-designed metastructures that solve equations, Science **363**, 1333 (2019).

[10] T. Zhu, Y. Zhou, Y. Lou, H. Ye, M. Qiu, Z. Ruan, *et al.*, Plasmonic computing of spatial differentiation, Nat. Commun. **8**, 15391 (2017).

[11] A. Pors, M. G. Nielsen, and S. I. Bozhevolnyi, Analog computing using reflective plasmonic metasurfaces, Nano Lett. **15**, 791 (2015).

[12] S. Abdollahramezani, O. Hemmatyar, and A. Adibi, Meta-optics for spatial optical analog computing, Nanophotonics **9**, 4075 (2020).

[13] H. Zhang, M. Gu, X. D. Jiang, J. Thompson, H. Cai, S. Paesani, *et al.*, An optical neural chip for implementing complex-valued neural network, Nat. Commun. **12**, 457 (2021).

[14] A. Silva, F. Monticone, G. Castaldi, V. Galdi, A. Alù, and N. Engheta, Performing mathematical operations with metamaterials, Science **343**, 160 (2014).

[15] M. Camacho, B. Edwards, and N. Engheta, A single inverse-designed photonic structure that performs parallel computing, Nat. Commun. **12**, 1466 (2021).

[16] Q. Tan, C. Qian, T. Cai, B. Zheng, and H. Chen, Solving multivariable equations with tandem metamaterial kernels, Prog. Electromagn. Res. **175**, 139 (2022).

[17] Y. Zuo, B. Li, Y. Zhao, Y. Jiang, Y.-C. Chen, P. Chen, *et al.*, All-optical neural network with nonlinear activation functions, Optica **6**, 1132 (2019).

[18] X. Lin, Y. Rivenson, N. T. Yardimci, M. Veli, Y. Luo, M. Jarrahi, *et al.*, All-optical machine learning using diffractive deep neural networks, Science **361**, 1004 (2018).

[19] C. Qian, X. Lin, X. Lin, J. Xu, Y. Sun, E. Li, *et al.*, Performing optical logic operations by a diffractive neural network, Light Sci. Appl. **9**, 59 (2020).

[20] M. Miscuglio, Y. Gui, X. Ma, Z. Ma, S. Sun, T. El Ghazawi, *et al.*, Approximate analog computing with metatronic circuits, Commun. Phys. **4**, 51 (2021).

[21] E. Feigenbaum, S. P. Burgos, and H. A. Atwater, Programming of inhomogeneous resonant guided wave networks, Opt. Express **18**, 25584 (2010).

[22] Q. Tan, C. Qian, and H. Chen, Inverse-designed metamaterials for on-chip combinational optical logic circuit, Prog. Electromagn. Res. **176**, 55 (2023).

[23] S. P. K. Anguluri, S. R. Banda, S. V. Krishna, S. Swarnakar, and S. Kumar, The design, analysis, and simulation of an optimized all-optical AND gate using a Y-shaped plasmonic waveguide for high-speed computing devices, J. Comput. Electron **20**, 1079 (2021).

[24] B. E. A. Saleh and M. C. Teich, *Fundamentals of Photonics* (John Wiley & Sons, Inc., New York, USA, 1991).

[25] J. Huang, H. Ma, D. Chen, H. Yuan, J. Zhang, Z. Li, *et al.*, Digital nanophotonics: The highway to the integration of subwavelength-scale photonics Ultra-compact, multi-function nanophotonic design based on computational inverse design, Nanophotonics **10**, 1011 (2021).

[26] R. Ding, T. Baehr-Jones, T. Pinguet, J. Li, N. C. Harris, M. Streshinsky, *et al.*, in *Optics InfoBase Conference Papers, Los Angeles: OSA Technical Digest* (Optica Publishing Group, 2012); 2012.

[27] N. Stroev and N. G. Berloff, Analog photonics computing for information processing, inference, and optimization, Adv. Quantum. Technol. **6**, 2300055 (2023).

[28] F. Zangeneh-Nejad and R. Fleury, Topological analog signal processing, Nat. Commun. **10**, 2058 (2019).

[29] F. Zangeneh-Nejad, D. L. Sounas, A. Alù, and R. Fleury, Analogue computing with metamaterials, Nat. Rev. Mater. **6**, 207 (2021).

[30] C. J. Smyth, Nonblocking photonic switch networks, IEEE J. Sel. Areas Commun. **6**, 1052 (1988).

[31] H. Liu, E. Bouillet, D. Pendarakis, N. Komaee, J. F. Labourdette, and S. Chaudhuri, Distributed route computation and provisioning in shared mesh optical networks, IEEE J. Sel. Areas Commun. **22**, 1626 (2004).

[32] R. Srinivasan and A. K. Somani, A generalized framework for analyzing time-space switched optical networks, IEEE J. Sel. Areas Commun. **20**, 202 (2002).

[33] D. C. Tzarouchis, B. Edwards, and N. Engheta, Programmable wave-based analog computing machine: a metastructure that designs metastructures, arXiv:2301.02850 (2022).

[34] A. Yakovlev and V. Pacheco-Peña, Enabling high-speed computing with electromagnetic pulse switching, Adv. Mater. Technol. **5,** 1 (2020).

[35] D. Pozar, *Microwave Engineering* (John Wiley & Sons, Inc., Hoboken, NJ, United States, 2011), 4th ed.

[36] R. G. MacDonald, A. Yakovlev, and V. Pacheco-Peña, Amplitude-controlled electromagnetic pulse switching using waveguide junctions for high-speed computing processes, Adv. Intell. Syst. **4,** 2200137 (2022).

[37] E. Feigenbaum and M. Orenstein, Perfect 4-way splitting in nano plasmonic X-junctions, Opt. Express **15,** 17948 (2007).

[38] S. Sun, M. Miscuglio, X. Ma, Z. Ma, C. Shen, E. Kayraklioglu, *et al.*, Induced homomorphism: Kirchhoff's law in photonics, Nanophotonics **10,** 1711 (2021).

[39] E. Feigenbaum and H. A. Atwater, Resonant guided wave networks, Phys. Rev. Lett. **104,** 147402 (2010).

[40] E. Feigenbaum and H. A. Atwater, Dielectric based resonant guided wave networks, Phys. Rev. Lett. **20,** 10674 (2012).

[41] R. Glyn MacDonald, A. Yakovlev, and V. Pacheco-Peña, Time derivatives via interconnected waveguides, Sci. Rep. **13,** 1 (2023).

[42] V. Pacheco-Peña and A. Yakovlev, in *Handbook of Unconventional Computing*, edited by A. Adamatzky (World Scientific, London, UK, 2021), pp. 465–492.

[43] Z. Zhou and Y. Li, N-port equal/unequal-split power dividers using epsilon-near-zero metamaterials, IEEE Trans. Microw. Theory Tech. **69,** 1529 (2021).

[44] See Supplemental Material at http://link.aps.org/supplemental/10.1103/PhysRevApplied.21.054054 for the following: (1) Junction waveguides without outer waveguides: nonperfect splitting. (2) Phase plots: four-port interconnected waveguides for perfect splitting. (3) Full derivation for Y_J and $|S_{21}|$ plots with retrieved admittance. (4) Retrieval of parallel admittances: fitting model. (5) Retrieval of parallel admittances: optimization model. (6) Effect of length and height of junction waveguides: four-port junction.

[45] V. Pacheco-Peña, M. Beruete, P. Rodríguez-Ulibarri, and N. Engheta, On the performance of an ENZ-based sensor using transmission line theory and effective medium approach, New J. Phys. **21,** 1 (2019).

[46] M. Beruete, N. Engheta, V. Pacheco-Peña, and A. Phys Lett, Experimental demonstration of deeply subwavelength dielectric sensing with epsilon-near-zero (ENZ) waveguides, Appl. Phys. Lett. **120,** 081106 (2022).

[47] M. Silveirinha and N. Engheta, Tunneling of electromagnetic energy through subwavelength channels and bends using ε-near-zero materials, Phys. Rev. Lett. **97,** 157403 (2006).

[48] A. Alù, M. G. Silveirinha, and N. Engheta, Transmission-line analysis of ε-near-zero–filled narrow channels, Phys. Rev. E **78,** 016604 (2008).

[49] N. Kinsey, C. DeVault, A. Boltasseva, and V. M. Shalaev, Near-zero-index materials for photonics, Nat. Rev. Mater. **4,** 742 (2019).

[50] V. Pacheco-Peña, V. Torres, M. Beruete, M. Navarro-Cia, and N. Engheta, ε-near-zero (ENZ) graded index quasi-optical devices: Steering and splitting millimeter waves, J. Opt. **16,** 9 (2014).

[51] F. Zhang, K. Song, M. Fan, and Y. Fan, All-metal-waveguide power divider with high power-combining efficiency, J. Infrared Millim. Terahertz Waves **37** 258 (2015).

[52] D. A. Frickey, Conversions Between S, Z, Y, H, ABCD, and T parameters which are valid for complex source and load impedances, IEEE Trans. Microw. Theory Tech. **42,** 205 (1994).

[53] V. Torres, P. Rodríguez-Ulibarri, M. Navarro-Cía, and M. Beruete, Fishnet metamaterial from an equivalent circuit perspective, Appl. Phys. Lett. **101,** 1 (2012).

[54] R Macdonald, V Pacheco Peña, A Yakovlev, In Prep (2023) 2023.

[55] C. A. Balanis, *Antenna Theory - Analysis and Design* (John Wiley & Sons, Hoboken, NJ, United States, 2016), 4th ed.

[56] CST Studio Suite (2024). https://doi.org/https://events.3ds.com/technology-enhancement-highlights-high-frequency.

[57] M. A. Zaman and L. Hesselink, Plasmonic response of nano-C-apertures: Polarization dependent field enhancement and circuit model, Plasmonics **18,** 155 (2023).

[58] Ş. E. Kocabaş, G. Veronis, D. A. B. Miller, and S. Fan, Transmission line and equivalent circuit models for plasmonic waveguide components, IEEE J. Sel. Top. Quantum Electron. **14,** 1462 (2008).

[59] J. Redden, *Advanced Algebra. 1.0* (Creative Commons, Visalia, California, 2012).

[60] B. Nijholt, J. Wetson, J. Hoofwijk, and A. Akhmerov, *Adaptive: Parallel active learning of mathematical functions* (Zenodo), 2019. https://doi.org/10.5281/zenodo.1182437.

[61] P. Virtanen, R. Gommers, T. E. Oliphant, M. Haberland, T. Reddy, D. Cournapeau, *et al.*, SciPy 1.0: Fundamental algorithms for scientific computing in Python. Nat. Methods 17 261 (2020).

[62] M. Newville, T. Stensitzki, D. B. Allen, M. sRawlik, A. Ingargiola, and A. Nelson, Lmfit: Non-linear least-square minimization and curve-fitting for Python (2016).